

Hyperspectral Imaging of Structure and Composition in Atomically Thin Heterostructures

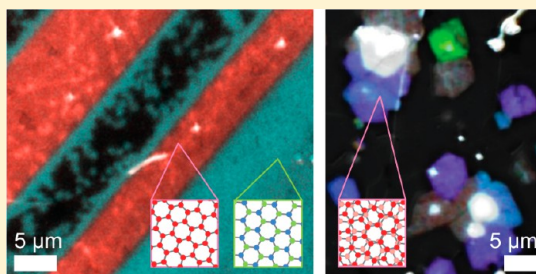
Robin W. Havener,[†] Cheol-Joo Kim,[‡] Lola Brown,[‡] Joshua W. Kevek,[§] Joel D. Sleppy,[†] Paul L. McEuen,^{§,||} and Jiwoong Park^{*,‡,||}

[†]School of Applied and Engineering Physics, [‡]Department of Chemistry and Chemical Biology, [§]Laboratory for Atomic and Solid State Physics, and ^{||}Kavli Institute at Cornell for Nanoscale Science, Cornell University, Ithaca, New York 14853, United States

S Supporting Information

ABSTRACT: Precise vertical stacking and lateral stitching of two-dimensional (2D) materials, such as graphene and hexagonal boron nitride (h-BN), can be used to create ultrathin heterostructures with complex functionalities, but this diversity of behaviors also makes these new materials difficult to characterize. We report a DUV–vis–NIR hyperspectral microscope that provides imaging and spectroscopy at energies of up to 6.2 eV, allowing comprehensive, all-optical mapping of chemical composition in graphene/h-BN lateral heterojunctions and interlayer rotations in twisted bilayer graphene (tBLG). With the addition of transmission electron microscopy, we obtain quantitative structure–property relationships, confirming the formation of interfaces in graphene/h-BN lateral heterojunctions that are abrupt on a micrometer scale, and a one-to-one relationship between twist angle and interlayer optical resonances in tBLG. Furthermore, we perform similar hyperspectral imaging of samples that are supported on a nontransparent silicon/SiO₂ substrate, enabling facile fabrication of atomically thin heterostructure devices with known composition and structure.

KEYWORDS: Graphene, hexagonal boron nitride, optical spectroscopy, optical microscopy



The controlled fabrication of two-dimensional heterostructures represents an exciting development in the field of 2D materials,^{1–7} because the additional structural and compositional degrees of freedom in these new materials allow their properties to be customized over a large energy range.⁸ Recent advances in this area include the fabrication of graphene/h-BN lateral heterojunctions using a patterned regrowth technique^{1,2} and vertical stacks of exfoliated 2D crystals using aligned transfers.^{4–7} In these examples, the composition changes across the lateral and/or vertical junctions (Figure 1a), and the uncontrolled crystal orientation of each stacked layer introduces additional spatial heterogeneity (Figure 1b). While transmission electron microscopy (TEM) techniques have allowed detailed imaging and characterization of these materials,^{1,2,5,9–11} the sample preparation requirements make subsequent device fabrication challenging; thus, 2D heterostructure devices with known composition and structure are currently difficult to produce on a large scale.

Optical microscopy provides a powerful platform for bridging this gap. The optical spectrum of a single-layer 2D material can be used to identify its composition: graphene,^{12–14} MoS₂,¹⁵ and h-BN¹⁶ have different band gap energies ranging from 0 (graphene) to over 6 eV (h-BN). In multilayer stacks, interlayer interactions can generate additional structure-dependent optical features.^{15,17–22} An important example is tBLG, which exhibits an extra absorption peak with a predicted energy between 0 and 4 eV, depending on its twist angle (θ).^{19–22} However, previous studies could not distinguish these optical signatures in

heterostructures with microscopic features due to limited spectral range (especially at deep ultraviolet (DUV) wavelengths) or limited imaging capabilities.

Here, we report hyperspectral imaging of 2D heterostructures, specifically, graphene/h-BN lateral junctions and tBLG, with a DUV–vis–NIR microscope that operates over the entire spectral range of 1.2 to 6.2 eV while maintaining submicrometer spatial resolution. It produces transmission or reflection images (see Figure 1c for transmission mode, Figure 5a for reflection mode) with no chromatic aberrations due to its exclusively mirror-based (“catoptric”)²³ optics; additionally, elements were specifically chosen for optimal performance over all DUV–vis–NIR energies (see Supporting Information). The graphene/h-BN lateral junctions studied in our work were produced by the patterned regrowth method¹ and are supported either by 10 nm thick silicon nitride (SiN) membranes¹⁰ for both optical and TEM imaging or by silicon substrates with thermal oxide. The tBLG studied in our work is grown by a chemical vapor deposition (CVD) technique and similarly prepared for measurements^{10,20} (for sample fabrication, see Supporting Information).

In Figures 2 and 3, we first study graphene/h-BN lateral heterostructures. Figure 2a shows optical transmission images of a graphene/h-BN lateral heterojunction on SiN with distinct,

Received: June 6, 2013

Revised: July 9, 2013

Published: July 10, 2013

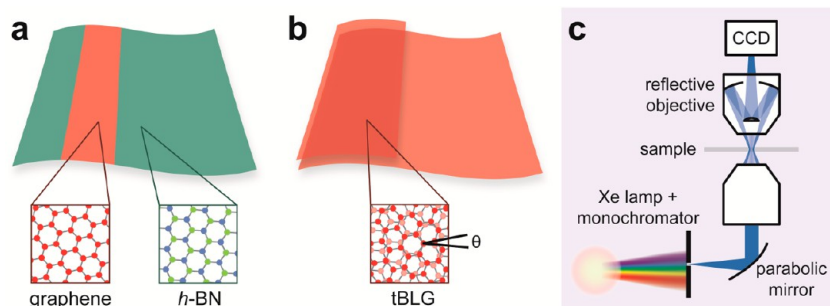


Figure 1. Schematics of (a) lateral and (b) vertical interfaces formed by graphene and h-BN. For the case of vertical stacking, the relative angle between the layers (θ) adds an additional degree of freedom. (c) Schematic of our DUV-vis-NIR hyperspectral microscope, which can measure spectral features from 1.2 to 6.2 eV with submicrometer spatial resolution and no chromatic aberrations.

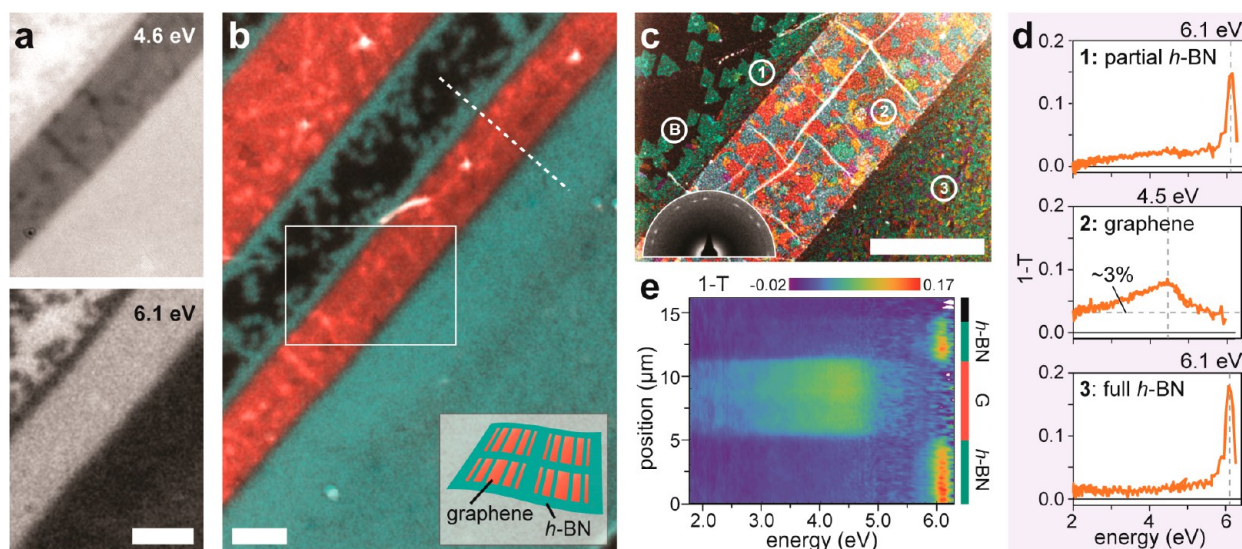


Figure 2. (a) Optical transmission images of a graphene/h-BN lateral heterostructure at two different energies, showing energy-dependent features. (b) False color image combining the images from (a), showing a clear stripe pattern which matches the (inset) intended design. (c) DF-TEM image of the same sample (from boxed region in (b)), showing the grain structure of the materials present, which reveals a clear junction. (inset) A representative background subtracted diffraction pattern from a junction region of the same sample, showing diffraction spots consistent with both graphene and h-BN. (d) Transmission spectra from three numbered regions outlined in (c) (with respect to the bare substrate, “B”), corresponding to partial and full h-BN growth and graphene. (e) Transmission spectra taken along the dashed line in (b), showing clear h-BN and graphene strips with little compositional mixing. All scale bars are 5 μm .

energy dependent features. Different regions appear darker (with reduced transmission) at 4.6 and 6.1 eV, which correspond to the known absorption peaks of graphene^{13,14} and h-BN,¹⁶ respectively. Because our microscope has no chromatic aberrations, such images can be easily combined to generate a false color composite, as shown in Figure 2b. This large-scale image reveals lateral junctions whose pattern matches the intended design (Figure 2b, inset) and suggests areas of both full and partial h-BN growth immediately adjacent to graphene strips. The junction formation is confirmed by a DF-TEM⁹ image (Figure 2c) of same device from Figure 2b (boxed region) in which different colors indicate domains of different crystalline orientations. This image shows clear lines across which the domain structure changes abruptly and confirms that both graphene and h-BN are polycrystalline single layers. We note, however, that our DF-TEM data alone cannot definitively distinguish between graphene and h-BN, because the diffraction patterns from both materials have the same symmetry and very similar lattice constants, as shown in a diffraction pattern from a junction region containing both materials (Figure 2c, inset).

The spatially resolved atomic composition is confirmed by full spectral measurements (Figure 2d,e). Figure 2d shows transmission spectra taken from several 1 μm diameter spots (outlined in Figure 2c), extracted from hundreds of transmission images of the same region measured while continuously varying the photon energy from 1.8 to 6.2 eV. The majority of these hyperspectral images can be acquired within minutes with an acquisition time per frame of <1 s for wavelengths above 250 nm, increasing to 1–2 min near 200 nm. Here, we plot $1 - T$, the transmission contrast (T defined as I/I_0 , where I_0 is the transmission intensity through the bare substrate, and I is the intensity through the substrate plus sample), which is approximately equal to the absorption of the sample in most cases. Regions 1 and 3 exhibit a sharp, narrow peak near 6.1 eV, consistent with h-BN,¹⁶ while region 2 exhibits a broad, asymmetric peak near 4.5 eV with roughly constant $1 - T$ at lower energies, consistent with graphene.^{12–14} These results provide the most direct confirmation of our assignments of the composition in each area and suggest high qualities of graphene and h-BN. Furthermore, a two-dimensional plot of $1 - T$ versus energy

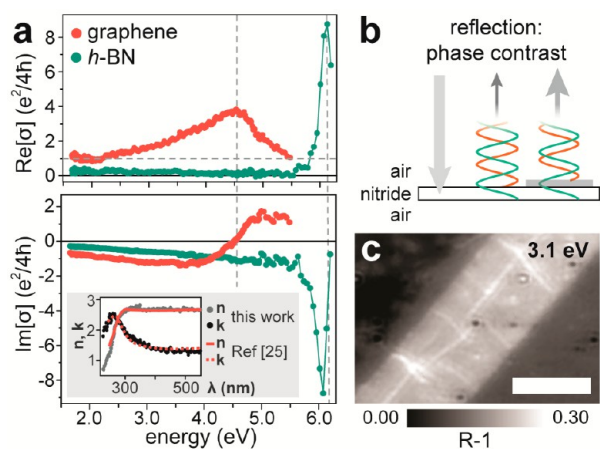


Figure 3. (a) Measured real and imaginary parts of the optical conductivity (σ) of single-layer CVD graphene and h-BN. (inset) Measured complex refractive index ($n + ik$) of CVD graphene (dots), compared with previous work (lines).²⁵ (b) Schematic illustrating phase contrast mechanism for reflection imaging of atomically thin films on a thin silicon nitride membrane (membrane thickness enlarged for clarity). (c) Reflection image of graphene/h-BN junction (same region as Figure 2c), showing that h-BN is visible far from its absorption peak in this mode (scale bar $5 \mu\text{m}$).

across the graphene/h-BN heterojunction (Figure 2e) suggests that the transition between the graphene and h-BN is abrupt on a micrometer scale, and that each region exhibits a homogeneous optical spectrum, suggesting little compositional

mixing. Thus, our graphene/h-BN heterostructure behaves as designed; additionally, we note that the optical response of the single-layer h-BN is similar for both partial and full growth regions with different grain structures, suggesting it is independent of grain size from hundreds of nanometers to $\sim 1 \mu\text{m}$.

Our microscope also provides quantitatively accurate, spatially resolved measurements of the complex optical conductivity (σ) of 2D materials (or permittivity, $\epsilon = i\sigma/\omega$). Figure 3a shows the real and imaginary parts of σ measured from our single-layer graphene and h-BN. These values were extracted from transmission and reflection images of the same sample and the known optical parameters and geometry of the SiN substrate (including material trapped under the 2D film, see Supporting Information). Interestingly, we find that while $1 - T$ of an atomically thin film on a thin ($\ll \lambda$) membrane is approximately proportional to the film's absorption (or $\text{Re}[\sigma]$), the reflection contrast $1 - R$ (where R is defined analogously to T) is instead approximately proportional to $\text{Im}[\sigma]$. This is because the reflections from the front and back of the thin membrane have opposite phase, interfering destructively;²⁴ the atomically thin film acts to alter this phase difference, typically increasing reflection, to a degree which depends on its thickness and dielectric constant (or $\text{Im}[\sigma]$) (Figure 3b). Because of this effect, h-BN is clearly visible in reflection mode even at low energies (Figure 3c). Additionally, small wrinkles in the graphene (white lines in Figures 2c and 3c) are easily visible in this imaging mode, compared with the transmission image in Figure 2b. Our data in Figure 3a provide complete quantitative

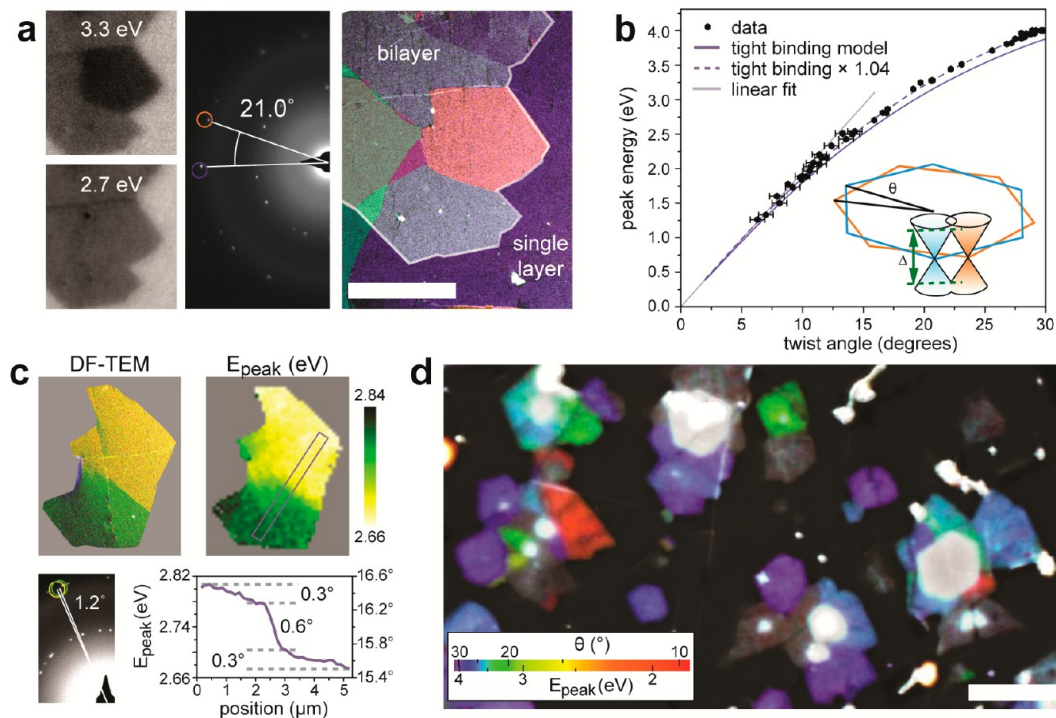


Figure 4. (a, left) Monochromatic optical images of one BLG sample showing a region of decreased transmission at 3.3 eV. (right) DF-TEM image resolving the structure and angle of the same area, confirming a tBLG domain of the same shape with $\theta = 21.0^\circ$ (scale bar $5 \mu\text{m}$). (b) E_{peak} versus θ measured for many tBLG domains for energies up to 4.1 eV, showing a clear monotonic relationship, along with fits and (inset) schematic of the theoretical model. Two data sets are plotted that have different uncertainties in θ , caused by differences in TEM alignment. (c) Comparison of DF-TEM (left) and pixel-by-pixel map of E_{peak} (right) for the same tBLG domain, illustrating that optical spectroscopy provides structural information with $\theta \sim 0.1^\circ$ precision. See main text for more details. (d) False color image of the resonance energies of many bilayer domains, illustrating the complex structure of tBLG grown by CVD (scale bar $10 \mu\text{m}$).

measurements of σ for single-layer h-BN for the first time and allow evaluation alongside that of CVD graphene. The full optical function we calculate for CVD graphene matches previous, Kramers–Kronig consistent measurements of its refractive index²⁵ ($n + ik = \epsilon^{1/2}$) (Figure 3a, inset). In comparison, $\text{Re}[\sigma]$ of single-layer h-BN peaks at $\sim 9 e^2/4\hbar$ (corresponding to $\sim 20\%$ absorption) for 6.11 ± 0.03 eV, and $|\text{Im}[\sigma]|$ peaks at a slightly lower energy with a similar height. Significantly, the accurate knowledge of σ for arbitrary atomically thin films enhances the capabilities of our microscope, because it allows us to predict the appearance of the same films on more complicated or nontransparent substrates for all-optical identification (see below, Figure 5).

Our data in Figures 2 and 3 clearly show that the DUV–vis–NIR hyperspectral microscope provides high-resolution imaging of the composition of lateral heterojunctions in atomically thin films. For single-layer graphene and h-BN, however, our measured σ is independent of structural features such as crystalline orientation and grain boundaries. On the other hand, this intrinsic σ may be modified due to structure dependent interlayer interactions when multiple layers are stacked. In Figure 4, we study tBLG, a prototypical multilayer system with one additional free structural parameter, the rotation angle θ .

Previous calculations²² predict that tBLG exhibits an optical absorption peak whose energy varies monotonically with θ over several electronvolts; however, this behavior has only been confirmed experimentally for a few domains over a small energy (1.4–3 eV) and θ (below 15°) range.^{19–21} Our hyperspectral optical imaging and TEM measurements provide a direct way to measure the optical properties of tBLG with known θ over a larger energy (1.2–6.2 eV) and θ (6 – 30°) range. As shown in Figure 4a, we find that distinct regions with decreased transmission appear in monochromatic images of CVD BLG. We confirm that these regions correspond to tBLG rotational domains, and measure their twist angle, by combining our optical measurements with DF-TEM. By repeating these measurements for many tBLG domains, we can correlate the peak absorption energy (E_{peak}) and θ , which is shown in Figure 4b. Consistent with theory,²² there is a monotonic, one-to-one relationship between E_{peak} and θ for the entire measured range of θ up to 30° .

A noninteracting band structure for tBLG, where two sets of single-layer electron bands are rotated relatively by θ (Figure 4b, inset), provides a simple model for this observation. These bands begin to intersect at two points, giving rise to singularities in the electronic joint density of states, and the energy difference between them (Δ) may be used to estimate E_{peak} .²⁰ This is plotted (solid line) as a function of θ using tight binding parameters calculated by Grüneis et al.²⁶ (GW fit), which provides an excellent fit to our data; empirically, slightly increasing (1.04 \times) the tight binding result gives the best fit (dashed line). We also observe that the relationship between E_{peak} and θ is almost linear at low energies due to graphene's linear band structure near the Dirac (K) point, and can be predicted using a simple equation, $E_{\text{peak}} = 2\hbar v_F k \sin(\theta/2)$, where $k = 1.70 \text{ \AA}^{-1}$ is the momentum of the K point and v_F the Fermi velocity of graphene.²⁷ $v_F = 0.96 \times 10^6$ m/s provides the best fit to our data in Figure 4d for $\theta < 12.5^\circ$.

The absorption peak energy E_{peak} is a robust probe of θ , allowing precise optical mapping of θ as a function of position with submicrometer resolution, as shown in Figure 4c. In a color composite DF-TEM image (Figure 4c, left), we examine a tBLG sample with $\theta \sim 16^\circ$, which has an additional low angle

($\Delta\theta < 1.2^\circ$) boundary between the upper and lower regions. More precise spatial mapping of θ with TEM would require collecting individual diffraction patterns from many small selected areas. However, this same feature is easily distinguished in a spatial map of E_{peak} of the same region (Figure 4c, top right), based on which we estimate $\Delta\theta$ to be a 0.6° using our fit in Figure 4b. Furthermore, we observe continuous spatial variations in θ of a few tenths of a degree away from the sharp boundary, as seen in a line cut (Figure 4c, bottom right) through the map of E_{peak} . These small variations in θ are consistent with previous DF-TEM studies of CVD-grown BLG¹⁰ and may be the result of local shear or strain during growth.

On a larger scale, a false color image mapping E_{peak} reveals the striking domain structure of our CVD BLG, and directly determines θ for all tBLG areas with optical resonances (Figure 4d). Currently, our microscope can measure optical features above 1.2 eV (corresponding to $\theta > 6^\circ$), limited by the poor infrared sensitivity of our CCD. By comparing our optical and TEM data, we observe that 90% area of BLG without an absorption peak is Bernal stacked, a reflection of the previously reported abundance of Bernal stacked, and lack of small θ , bilayer graphene in CVD samples.¹⁰

Our DUV–vis–NIR hyperspectral microscope can also image and characterize atomically thin heterostructures on nontransparent substrates for device fabrication, most notably silicon with an oxide layer, when operating in reflection mode (Figure 5a, inset). For monochromatic imaging, the oxide thickness determines the contrast once $\sigma(\lambda)$ of the atomically

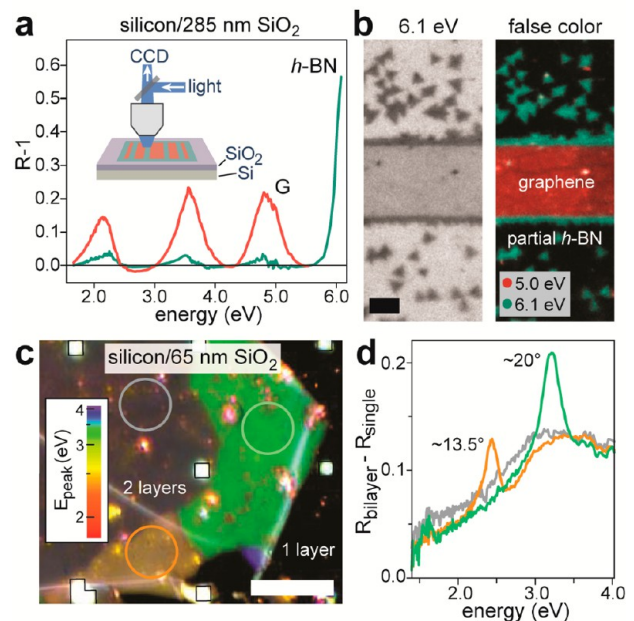


Figure 5. (a) Contrast ($R - 1$) of graphene and h-BN on Si/SiO₂ (285 nm) for energies of up to 6.1 eV, calculated using σ from Figure 3. (inset) Schematic for imaging samples on Si/SiO₂ substrates in reflection mode. (b) (left) Image of a graphene/h-BN junction on Si/SiO₂ (285 nm), illustrating that h-BN is clearly visible at 6.1 eV, and (right) a false color image combining data at 6.1 and 5.0 eV, showing the relative positions of graphene and h-BN in this device (scale bar 5 μm). (c) False color image of BLG on Si/SiO₂ (65 nm); the grid of white dots (outlined) are gold alignment marks for use in further device fabrication (scale bar 10 μm). (d) Reflection spectra of the regions circled in (c).

thin film is known.²⁸ We calculate $(R - 1)$ versus energy for graphene and h-BN on 285 nm thick oxide (widely used for graphene devices), based on our measured σ (Figure 3), in Figure 5a. It predicts high contrast for graphene near 2.2, 3.6, and 4.8 eV, while h-BN exhibits high contrast only near 6.1 eV. This allows rapid imaging of both graphene and h-BN directly on Si/SiO₂ (285 nm), as demonstrated in Figure 5b. We note that h-BN should be visible at 6.1 eV for most oxide thicknesses, including on bare silicon, except for a few specific cases (near $(54 + 66\alpha)$ nm, where α is an integer). Furthermore, decreasing the oxide thickness allows reflection spectroscopy over a broad range of energies by increasing the energy difference between zero contrast points (such as ~ 2.7 , 4.2, and 5.5 eV for single-layer graphene on 285 nm oxide in Figure 5a). Figure 5c shows a false color image (as in Figure 4d) of a BLG sample on Si/SiO₂ (65 nm), which resolves two colored tBLG domains and a gray, spectrally featureless (Bernal or small θ) BLG domain. Full reflection spectra between 1.4 and 4.1 eV from these regions are shown in Figure 5d, allowing us to determine θ (~ 13.5 and 20°) for both tBLG domains. This capability will allow the fabrication of electronic and optoelectronic devices based on individual tBLG domains with different θ as well as heterojunctions formed between them.

In conclusion, our DUV-vis-NIR hyperspectral microscope provides a versatile platform for imaging and characterization of arbitrary 2D heterostructures. While we focus on structures based on h-BN and graphene in this initial work, the optical and TEM characterization methods demonstrated here can be immediately applied for the study of heterostructures formed between other 2D materials, including BCN, MoS₂, and other metal dichalcogenides. Recent theoretical work has predicted exciting optical and electronic properties in many such systems which have yet to be characterized;^{29–31} our technique provides an essential tool for developing complex 2D devices with highly controlled, tunable functionalities.

■ ASSOCIATED CONTENT

📄 Supporting Information

Detailed description of the DUV-vis-NIR microscope, sample fabrication procedures, and method of calculating σ . This material is available free of charge via the Internet at <http://pubs.acs.org>.

■ AUTHOR INFORMATION

Corresponding Author

*E-mail: jpark@cornell.edu.

Notes

The authors declare no competing financial interest.

■ ACKNOWLEDGMENTS

The authors thank L. Huang, M. Wojcik, and M. P. Levendorf for help with sample synthesis and preparation, and M. W. Graham for useful discussions. This work was mainly supported by the AFOSR (Grants FA9550-09-1-0691, FA2386-10-1-4072) and the Samsung Advanced Institute for Technology GRO Program, as well as the Kavli Institute at Cornell for Nanoscale Science (KIC). Additional funding was provided by the NSF through the Cornell Center for Materials Research (NSF DMR-1120296) and the Nano Material Technology Development Program through the National Research Foundation of Korea (NRF) funded by the Ministry of Science, ICT, and Future Planning (2012M3A7B4049887).

R.W.H. was partially supported by an NSF Graduate Research Fellowship. C.-J.K. was partially supported by the Basic Science Research Program through the NRF funded by the Ministry of Education, Science and Technology (2012R1A6A3A03040952). Device fabrication was performed at the Cornell NanoScale Facility, a member of the National Nanotechnology Infrastructure Network, which is supported by the National Science Foundation (Grant ECS-0335765).

■ REFERENCES

- (1) Levendorf, M.; Kim, C.; Brown, L.; Huang, P.; Havener, R.; Muller, D.; Park, J. *Nature* **2012**, *488* (7413), 627–632.
- (2) Liu, Z.; et al. *Nat. Nanotechnol.* **2013**, *8*, 119–124.
- (3) Sutter, P.; Cortes, R.; Lahiri, J.; Sutter, E. *Nano Lett.* **2012**, *12* (9), 4869–4874.
- (4) Dean, C.; et al. *Nat. Nanotechnol.* **2010**, *5* (10), 722–726.
- (5) Haigh, S. J.; Gholinia, A.; Jalil, R.; Romani, S.; Britnell, L.; Elias, D. C.; Novoselov, K. S.; Ponomarenko, L. A.; Geim, A. K.; Gorbachev, R. *Nat. Mater.* **2012**, *11* (9), 747–767.
- (6) Britnell, L.; et al. *Nano Lett.* **2012**, *12* (3), 1707–1710.
- (7) Britnell, L.; et al. *Science* **2012**, *335* (6071), 947–950.
- (8) Neto, A.; Novoselov, K. *Rep. Prog. Phys.* **2011**, *74* (8), 082501.
- (9) Huang, P.; et al. *Nature* **2011**, *469* (7330), 389–392.
- (10) Brown, L.; Hovden, R.; Huang, P.; Wojcik, M.; Muller, D. A.; Park, J. *Nano Lett.* **2012**, *12*, 1609–1615.
- (11) Zhan, Y.; Liu, Z.; Najmaei, S.; Ajayan, P.; Lou, J. *Small* **2012**, *8* (7), 966–971.
- (12) Nair, R.; Blake, P.; Grigorenko, A.; Novoselov, K.; Booth, T.; Stauber, T.; Peres, N.; Geim, A. *Science* **2008**, *320* (5881), 1308–1308.
- (13) Chae, D.; Utikal, T.; Weisenburger, S.; Giessen, H.; von Klitzing, K.; Lippitz, M.; Smet, J. *Nano Lett.* **2011**, *11* (3), 1379–1382.
- (14) Mak, K.; Shan, J.; Heinz, T. *Phys. Rev. Lett.* **2011**, *106* (4), 046401.
- (15) Mak, K.; Lee, C.; Hone, J.; Shan, J.; Heinz, T. *Phys. Rev. Lett.* **2010**, *105* (13), 136805.
- (16) Kim, K.; et al. *Nano Lett.* **2012**, *12* (1), 161–166.
- (17) Mak, K. F.; Lui, C. H.; Shan, J.; Heinz, T. F. *Phys. Rev. Lett.* **2009**, *102* (25), 256405.
- (18) Zhang, Y.; Tang, T.; Girit, C.; Hao, Z.; Martin, M.; Zettl, A.; Crommie, M.; Shen, Y.; Wang, F. *Nature* **2009**, *459* (7248), 820–823.
- (19) Robinson, J. T.; Schmucker, S. W.; Diaconescu, C. B.; Long, J. P.; Culbertson, J. C.; Ohta, T.; Friedman, A. L.; Beechem, T. E. *ACS Nano* **2012**, *7*, 637.
- (20) Havener, R.; Zhuang, H.; Brown, L.; Hennig, R.; Park, J. *Nano Lett.* **2012**, *12* (6), 3162–3167.
- (21) Wang, Y.; Ni, Z.; Liu, L.; Liu, Y.; Cong, C.; Yu, T.; Wang, X.; Shen, D.; Shen, Z. *ACS Nano* **2010**, *4* (7), 4074–4080.
- (22) Moon, P.; Koshino, M. *Phys. Rev. B* **2013**, *87*, 205404.
- (23) Barker, R. *Philos. Trans.* **1735**, *39*, 259–261.
- (24) Overbeek, J. J. *Phys. Chem.* **1960**, *64* (9), 1178–1183.
- (25) Nelson, F.; Kaminen, V.; Zhang, T.; Comfort, E.; Lee, J.; Diebold, A. *Appl. Phys. Lett.* **2010**, *97* (25), 253110.
- (26) Gruneis, A.; Attacalite, C.; Wirtz, L.; Shiozawa, H.; Saito, R.; Pichler, T.; Rubio, A. *Phys. Rev. B* **2008**, *78* (20), 205425.
- (27) dos Santos, J.; Peres, N.; Castro, A. *Phys. Rev. Lett.* **2007**, *99* (25), 256802.
- (28) Blake, P.; Hill, E.; Neto, A.; Novoselov, K.; Jiang, D.; Yang, R.; Booth, T.; Geim, A. *Appl. Phys. Lett.* **2007**, *91* (6), 063124.
- (29) Yan, J.; Jacobsen, K. W.; Thygesen, K. S. *Phys. Rev. B* **2012**, *86* (3), 045208.
- (30) Košmider, K.; Fernández-Rossier, J. *Phys. Rev. B* **2012**, *87*, 075451.
- (31) Park, H.; Wadehra, A.; Wilkins, J.; Neto, A. *Appl. Phys. Lett.* **2012**, *100* (25), 253115.